# Fabrication of Zr-based Bulk Metallic Glass from Crystalline Foil Using Laser Foil Printing Process

Yu-Xiang Wang, Zhen-Jie Zhao, Hung-Chu Chiang, Chia-Hung Hung

*Department of Mechanical Engineering, National Cheng Kung University, Tainan, 701, Taiwan, R.O.C.*

## Abstract

In this study, the crystalline zirconium-based alloys foil was used to fabricate bulk metallic glass (BMG) by the laser-foil-printing (LFP) process. Through laser spot pattern welding, the crystalline phase of $NiZr_2$ and its oxides in Zr-based crystalline foil were remelted and disordered to form BMG parts. BMG parts fabricated from amorphous foil and crystalline foil were characterized and compared for the amorphous structure through X-Ray diffraction (XRD). The microhardness revealed similar mechanical properties of LFP-fabricated BMGs using different crystalline types of feedstocks. Moreover, in the transmission-electron-microscope (TEM) results of BMGs, the select area electron diffraction (SAED) pattern and the bright-field (BF) images show a typical amorphous structure, indicating the feasibility of using the crystalline foil.

## Keywords

additive manufacturing, bulk metallic glass, crystalline foil, laser foil printing

## 1. Introduction

Metallic glass (MG) is renowned for its outstanding glass-forming ability (GFA) and mechanical properties, including resistance to corrosion, high hardness, elasticity, and wear resistance. Due to its non-crystalline structures, the amorphous metal possesses no grains and grain boundaries, effectively avoiding defects commonly found in traditional crystalline metals. Nonetheless, creating an amorphous structure requires high cooling rates, a challenge often encountered with traditional processes. A study indicates that, in the die-casting process, crystallization of casting parts initiates when the diameter exceeds 5 mm [1]. Consequently, the fabrication of thick or intricate Bulk Metallic Glass (BMG) parts becomes challenging using conventional methods.

In recent times, additive manufacturing (AM) processes have gained recognition for fabricating intricate three-dimensional parts layer by layer. One such method, laser powder bed fusion (L-PBF), employs powder as feedstock. Due to the thin nature of the powder, this process commonly demonstrates elevated cooling rates in contrast to traditional methods. Consequently, numerous studies have delved into resolving

crystallization challenges in metallic glass. In various metallic glass materials, Zr-based metallic glass has been used as feedstock in AM processes due to its excellent glass forming ability (GFA). However, it has been revealed that Zr-based metallic glass is prone to crystallization [2]. Certain studies have indicated that in the L-PBF process, columnar crystals or nano-crystalline structures can form in the heat affected zone (HAZ) of the melt pool [3,4]. The emergence of these crystalline structures may result in a reduction of mechanical and physical properties, potentially leading to the formation of cracks within the columnar grains [5]. Hence, a process with a higher cooling rate must be developed to address this issue.

Recently, the innovative additive manufacturing technique, laser foil printing (LFP), has demonstrated its ability to successfully create bulk metallic glass (BMG) components through a layer-by-layer fabrication process using amorphous foil as feedstock, as highlighted in references [6-11]. The resulting parts maintain their amorphous structures, attributed to the heightened thermal conductivity of metal foils [12]. However, despite the LFP process's capability to fabricate BMG parts, obtaining the necessary amorphous foil remains a challenge. An investigation uncovered that utilizing traditional rolling processes at room temperature for fabricating metallic glass foil resulted in the occurrence of nano-crystallizations [13]. To generate the necessary amorphous foil, the melt spinning process was employed, facilitating the swift cooling of metallic glass from its molten state. The molten metal underwent rapid cooling at a rate of $10^6$ K/s, leading to the formation of smooth ribbons or sheets [14]. Nevertheless, acquiring amorphous foil proves to be both costly and challenging. In an attempt to diminish dependence on amorphous foil, this study aims to produce amorphous bulk metallic glass (BMG) by remelting crystalline foils using the LFP process through its rapid cooling properties.

To create the crystalline foil, the amorphous foil underwent heat treatment in a high-temperature furnace, being maintained for one hour at 500˚C to achieve complete crystallization. Two LFP parts were fabricated, one using amorphous foil and the other using crystalline foil, to discern the differences between them. The surfaces and elemental compositions of the samples were analyzed using scanning electron microscopy (SEM) and energy-dispersive X-ray spectroscopy (EDS). For a more comprehensive exploration of the amorphous structures, X-ray diffraction (XRD) and transmission electron microscopy (TEM) were employed to analyze the LFP parts fabricated with the two types of foils.

## 2. Experiment setup

### 2.1 LFP process

To weld and cut metal foil in the LFP process, two laser systems were employed, which are continuous-wave (CW) fiber laser (IPG YLR-1000-MM-WC, DE) and pulse laser (IPG YLPN-1-4x200-30-M, DE). The schematic figure is presented in Fig. 1. The CW fiber laser involved a galvo-mirror scanning system (SCANLAB, HurrySCAN 20) and an F-θ lens with 254 mm focal length (FTH-254-1064), with a maximum power output of 1000 W. To prevent the crystallization of bulk metallic glass (BMG), the foil fixing and pattern welding were executed with a negative defocus of 6 mm from the foil surface, employing a laser spot size (d) of 170 μm. The pulse laser has a maximum power output of 30 W with an F-θ lens of 125 mm focal length, focusing on the foil surface. The center wavelength for both lasers is 1064 nm.

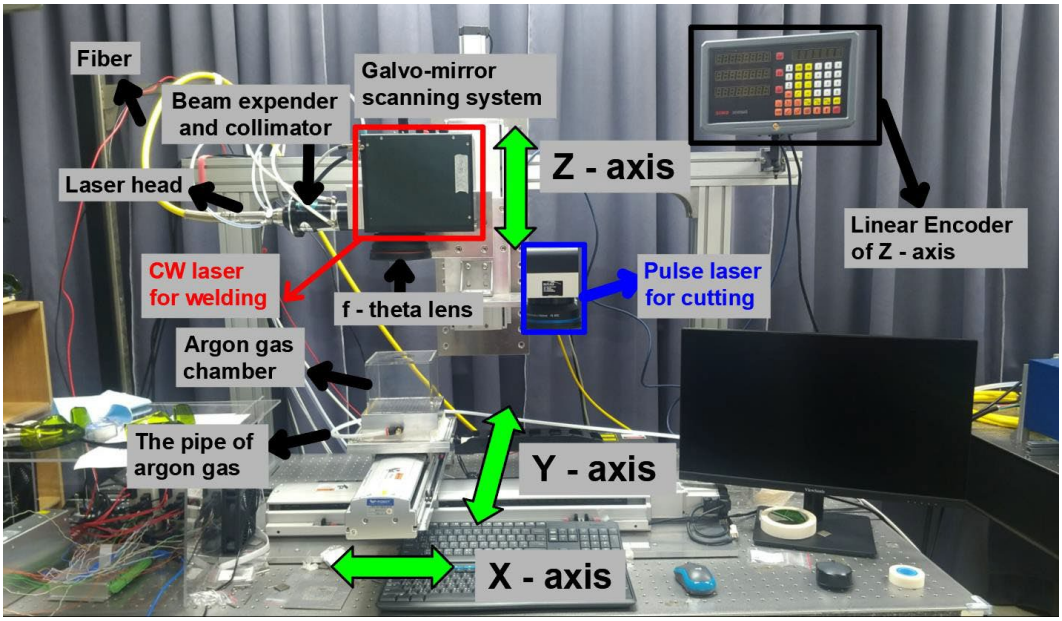


**Fig. 1** Schematic of LFP process system.

To fabricate LFP part, there are five steps involved in each layer, as illustrated in Fig. 2. First, the metal foil was slightly polished with 400# sandpaper to remove surface defects, followed by ethanol cleaning to remove any potential oxidation. Secondly, the foil fixing was conducted with the CW fiber laser and a spot distance of 1 mm to prevent foil distortion, as shown in Fig. 2(b). Thirdly, the pattern scanning was separated into two different sections, as illustrated in Fig. 3. The foil contour is welded first, followed by welding the center section. The welded spot distance was set to 150 μm for each neighboring point. Throughout the scanning process, the spacing between the next welded spot was maintained at 3 mm to prevent heat accumulation and crystallization. The pattern scanning was done in the argon chamber to preventing oxidation and

crystallization. After finished the pattern scanning, a pulse laser was utilized to cut the contour and remove excess foil, as shown in Fig. 2(d) and (e). Finally, the welded surface was polished with 400# sandpaper to enhance attachment with the next layer, as shown in Fig. 2(f). In pattern welding, each spot utilized a 500 W laser power with a 0.65 ms spot duration. The time elapsed between two spots was 125 ms. The zirconium 702 was applied for substrate with dimensions of 25 x 25 x 5 $mm^3$. And the thickness of $Zr_{52.5}Cu_{17.9}Ni_{14.6}Al_{10}Ti_5$ (at.%) (Liquidmetal®, LM105) amorphous foil was 200 μm for each layer. The crystalline foil was produced from the amorphous foil using a high-temperature furnace, followed by a 1-hour heat treatment at 500˚C conducted in a vacuum environment. This process aimed to induce crystallization in the foil and prevent excessive oxidation. Once the foil had crystallized, it was remelted to become an amorphous part through the LFP process, as illustrated in Fig. 4.

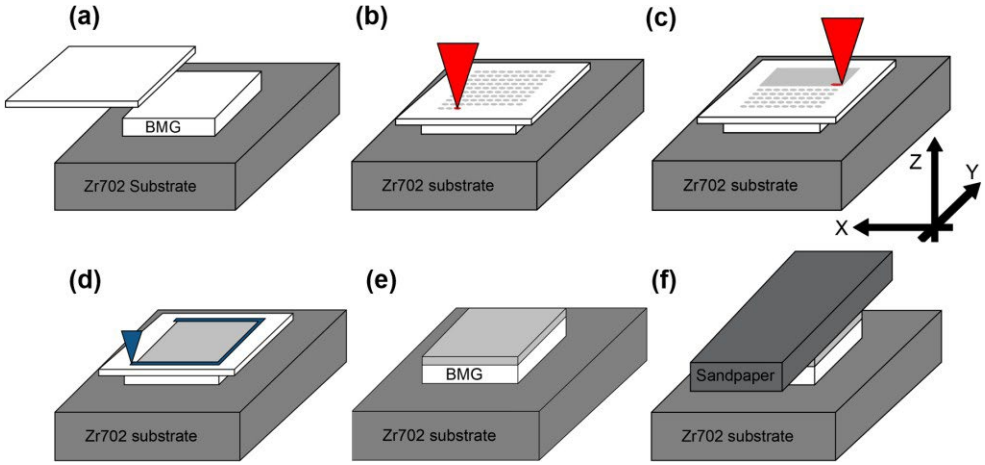


**Fig. 2** Schematic of five steps in LFP process (a)foil feeding (b)foil fixing (c)spot pattern scanning (d)contour cutting (e)excess foil remove (f)surface polishing.

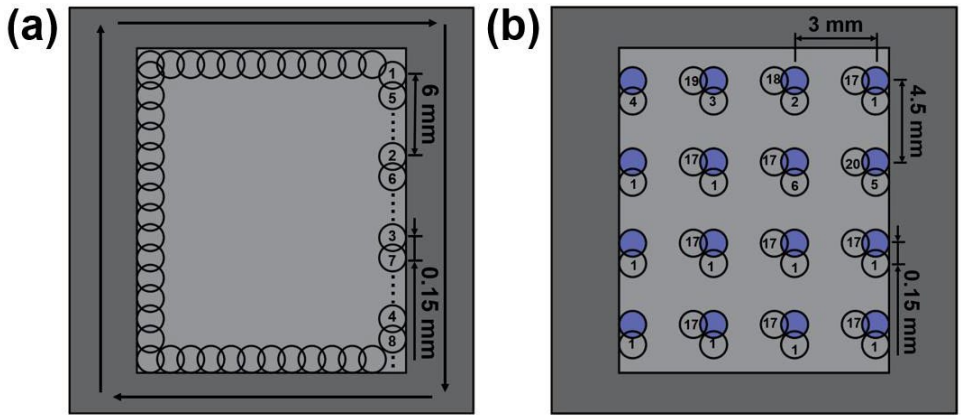


**Fig. 3** Pattern scanning path of (a) contour welding, (b) center welding.

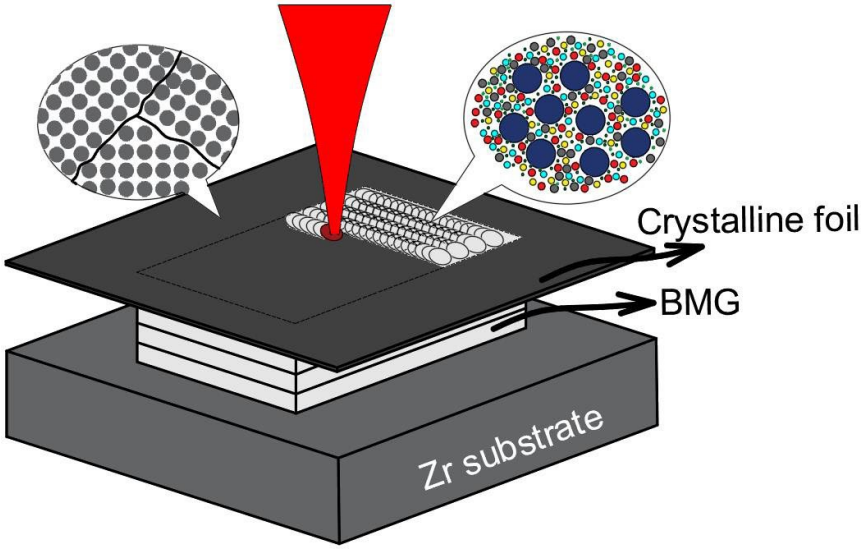


**Fig. 4** Schematic of the crystalline foil remelted into BMG part.

### 2.2 Material Characterization

Two samples fabricated by amorphous and crystalline foil were analyzed. The welded surface and cross-section were observed using an optical microscope (OM, Vitiny-UM20, Taiwan). Specimen cross sections were polished by #200, #400, #800, #1200, #2000, #4000 sandpaper, and followed by 1, 0.3, 0.05 μm aluminum oxide suspension, then characterized by a scanning electron microscope (SEM, Hitachi SU-8000, JP). An energy dispersive X-ray spectroscopy (EDS, Bruker XFlash 5010) was used to characterize element contents. Microhardness was tested on Vickers hardness tester (HMV-G31S, JP) with loading of 490.3 mN for 15 seconds holding time. Relative density was determined from SEM images, and the percentage of pores was measured using ImageJ software for a total area size of 9 $mm^2$. The crystalline phase and amorphous structure were analyzed with X-ray diffraction equipment (XRD, Bruker D8D Plus-TXS, DE) and X'pert software (version 3.0) with a PDF 2004 database. To thoroughly confirm the of the fabricated part derived from crystalline foils, a focused ion beam (FIB, FEI Nova-200 NanoLab) was used to prepare the sample. Subsequently, the prepared sample were loaded into a transmission electron microscope (TEM, JEOL TEM-2100F) to characterize the atomic structures.

## 3. Results

### 3.1 Characterization of LM105 foil

Fig. 5(a) displays the received original foil surface. To maintain the amorphous structure, a melt spinning process was applied. However, due to the manufacturing conditions, numerous pores formed on the foil surface. To mitigate the impact of these pores, all foil surfaces were grinded, as depicted in Fig. 5(b). The grinded surfaces of both amorphous and crystalline foils are shown in Fig. 6. The crystallinity and element contents of the two foils were characterized, as illustrated in Fig. 7 and table 1.

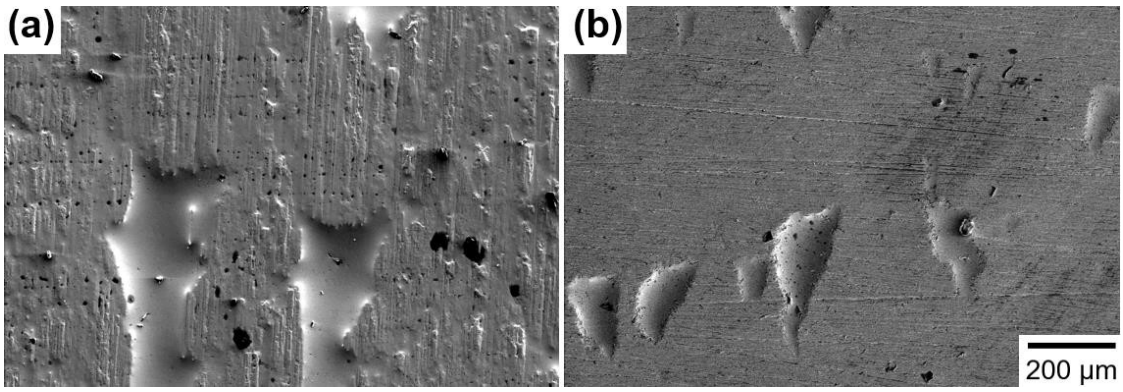


**Fig. 5** SEM images of (a) original, (b) grinded amorphous foil surface

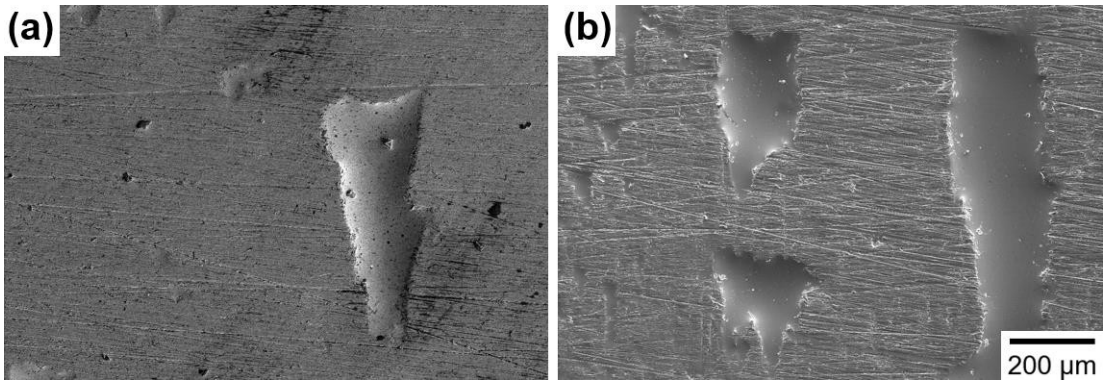


**Fig. 6** SEM images of (a) amorphous, (b) crystalline LM105 foil surface.

Following heat treatment, the FCC phase of $NiZr_2$ (space group $FD\bar{3}M$) formed at 453˚C, leading to increased embrittlement of the crystalline foil [15]. According to the EDS results, the crystalline foil exhibited a significant rise in oxygen content from 2.51 to 10.18 wt.%. This increase contributed to various oxidations observed in the XRD pattern, resulting in ductility loss and a microhardness increase from 555.8 ± 32.28 HV to 733 ± 8.75 HV.

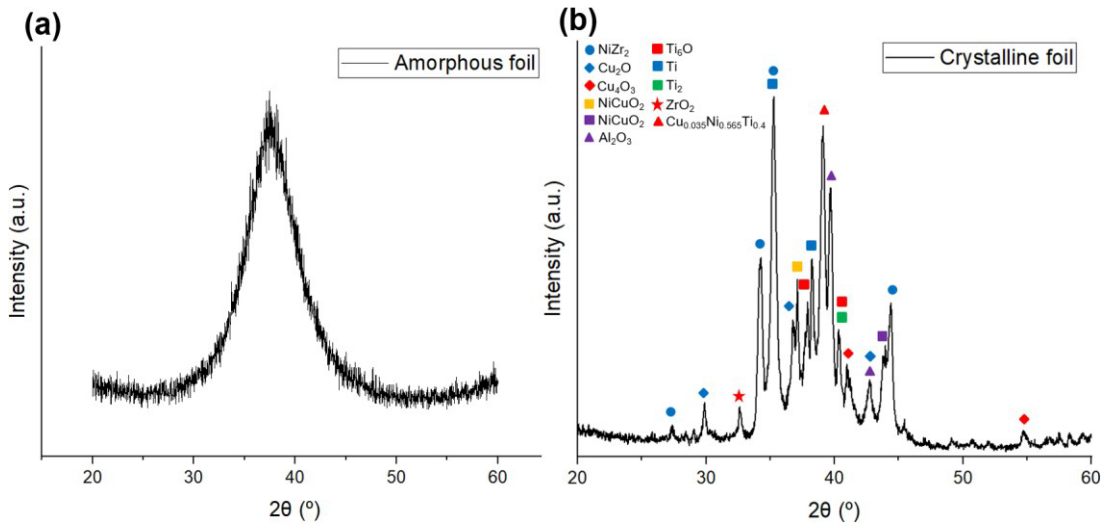


**Fig. 7** XRD results of (a) amorphous foil, (b) crystalline foil.

**Table 1** Element contents (wt.%) of amorphous and crystalline foil.

| **Element** | Zr | Cu | Ni | Ti | Al | O |
|---|---|---|---|---|---|---|
| Amorphous foil | 57.39 | 14.74 | 10.69 | 3.36 | 3.09 | 2.51 |
| Crystalline foil | 55.91 | 14.11 | 10.29 | 3.14 | 3.02 | 10.18 |

### 3.2 Characterization of BMG

Fig. 8 shows the LFP-fabricated bulk metallic glass (BMG) part. Four layers were achieved with a 500 W laser power and a 0.65 ms spot time duration of laser spot welding. The average welded spot size was 563 μm. In Fig. 9(a) and (c), the BMG surface from the amorphous foil exhibits uniformly welded spots. However, in Fig. 9(b) and (d), the BMG surface from the crystalline foil shows some surface protrusions. The thermal properties underwent significant changes due to crystallization [16]. After the amorphous foil crystallized, there was a decrease in glass-forming ability (GFA), potentially leading to surface defects on the BMG part.

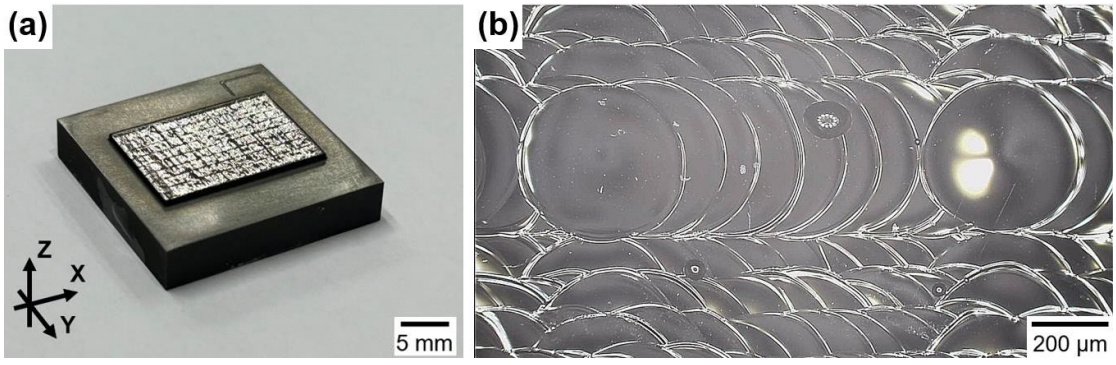


**Fig. 8** OM images of (a) LFP-fabricated BMG, (b) BMG top surface

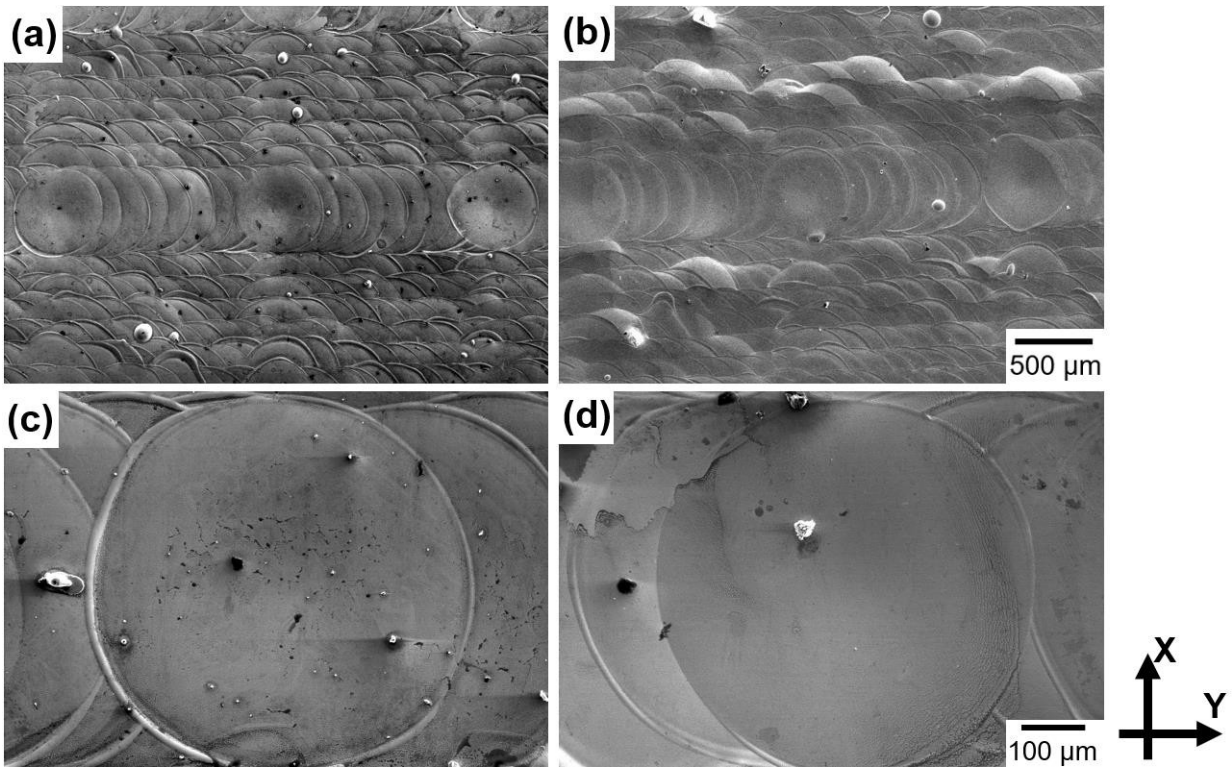


**Fig. 9** SEM images of LPF-fabricated BMG from (a,c) amorphous foil, (b,d) crystalline foil.

Fig. 10 presents the cross sections of BMG fabricated from amorphous and crystalline foil, with their relative densities of 99.25% and 98.7%, respectively. While the BMG from the crystalline foil exhibits a relatively rough surface and higher pore formation, both BMG parts show amorphous structures in XRD patterns, as depicted in Fig. 11. Table 2 displays the EDS analysis of the two BMG parts. Both BMG parts exhibit similar element contents, indicating that oxidations and crystalline phases were remelted into the amorphous part, followed by rapid cooling with a higher cooling rate of over 10 K/s to fabricate amorphous structures.

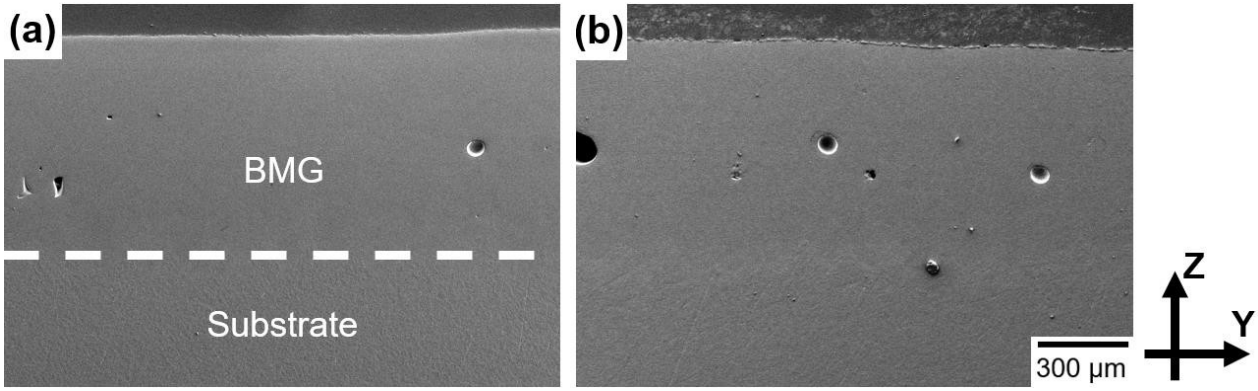


**Fig. 10** Cross sections of LFP-fabricated BMG from (a) amorphous foil, (b) crystalline foil.

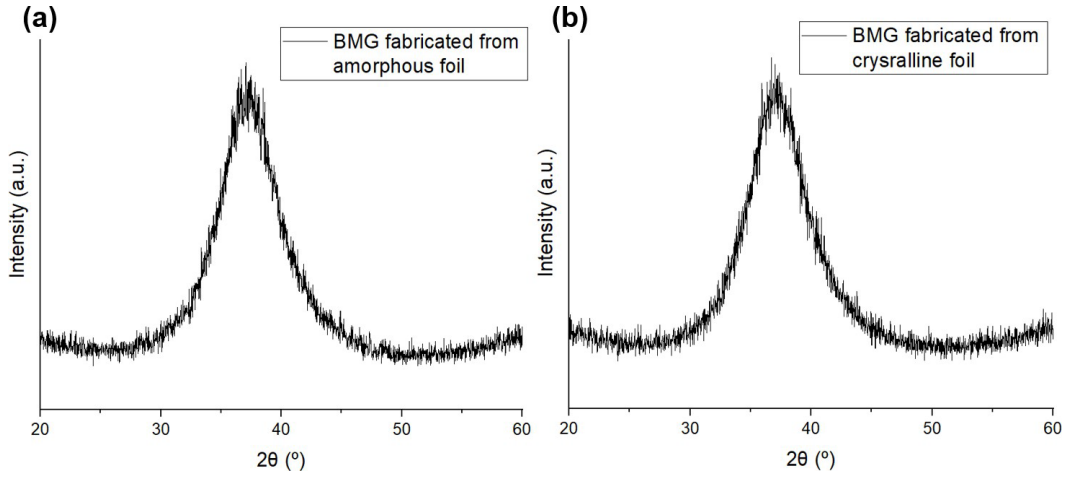


**Fig. 11** XRD results of LFP-fabricated BMG from (a) amorphous foil, (b) crystalline foil.

**Table 2** Element contents (wt.%) of LFP-fabricated BMG from amorphous and crystalline foil.

| **Element** | Zr | Cu | Ni | Ti | Al | O |
|---|---|---|---|---|---|---|
| BMG fabricated from amorphous foil | 65.02 | 12.18 | 10.44 | 3.17 | 2.63 | 5.01 |
| BMG fabricated from crystalline foil | 63.94 | 10.83 | 9.18 | 3.06 | 2.49 | 5.06 |

In the microhardness test, two BMG parts were examined along the spot-welded cross sections. Both samples exhibited similar values due to the same fabrication process, indicating comparable mechanical properties. The average microhardness of the two BMG samples was around 490 HV, as shown in Fig. 12. Test points were evaluated along the substrate, melt pool, and BMG region, with microhardness increasing from 140 HV to 490 HV as the test point reached the amorphous region. In the intermediate region between the substrate and the first layer, the hardness was around 206 HV, primarily caused by the high content of zirconium, which generated the α-Zr phase and softened the BMG [10].

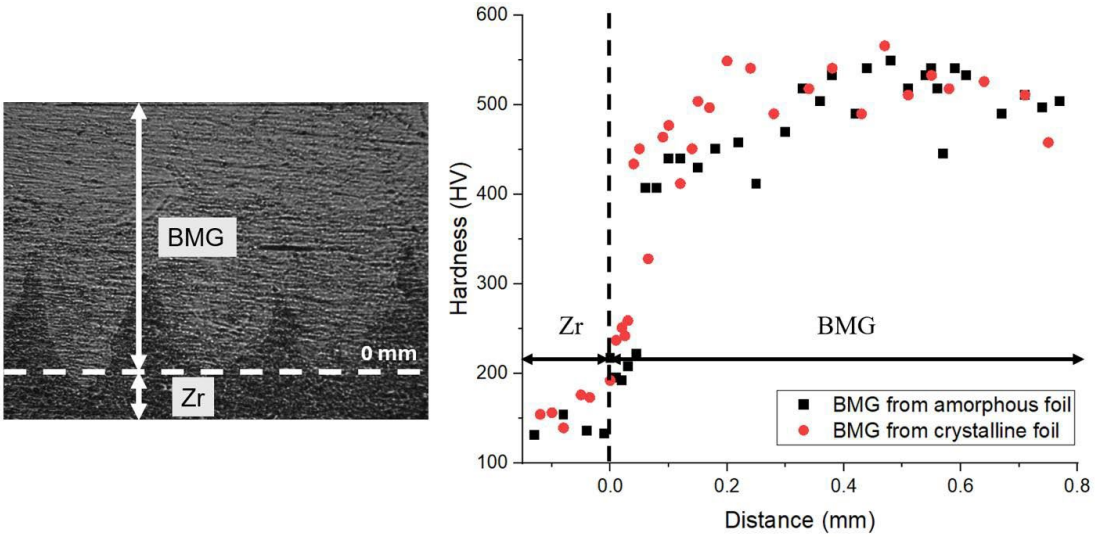


**Fig. 12** Microhardness of LFP-fabricated BMG from amorphous and crystalline foil.

To further examine the possible nanocrystals that may not be detectable by XRD in the amorphous structure, the sample was cut from BMG fabricated from crystalline foils through the focused ion beam (FIB) process. Then fixed onto half-moon grids for TEM analysis, as shown in Fig. 13(a). In Fig. 13(c) and (d), the magnification of 400,000x and 800,000x bright-field (BF) images of the BMG sample is presented. Both BF images do not exhibit a long-range ordered phase or crystalline lattice. The inset select area electron diffraction (SAED) pattern in BF images presents a halo ring, which is indicative of the typical amorphous structure [17].

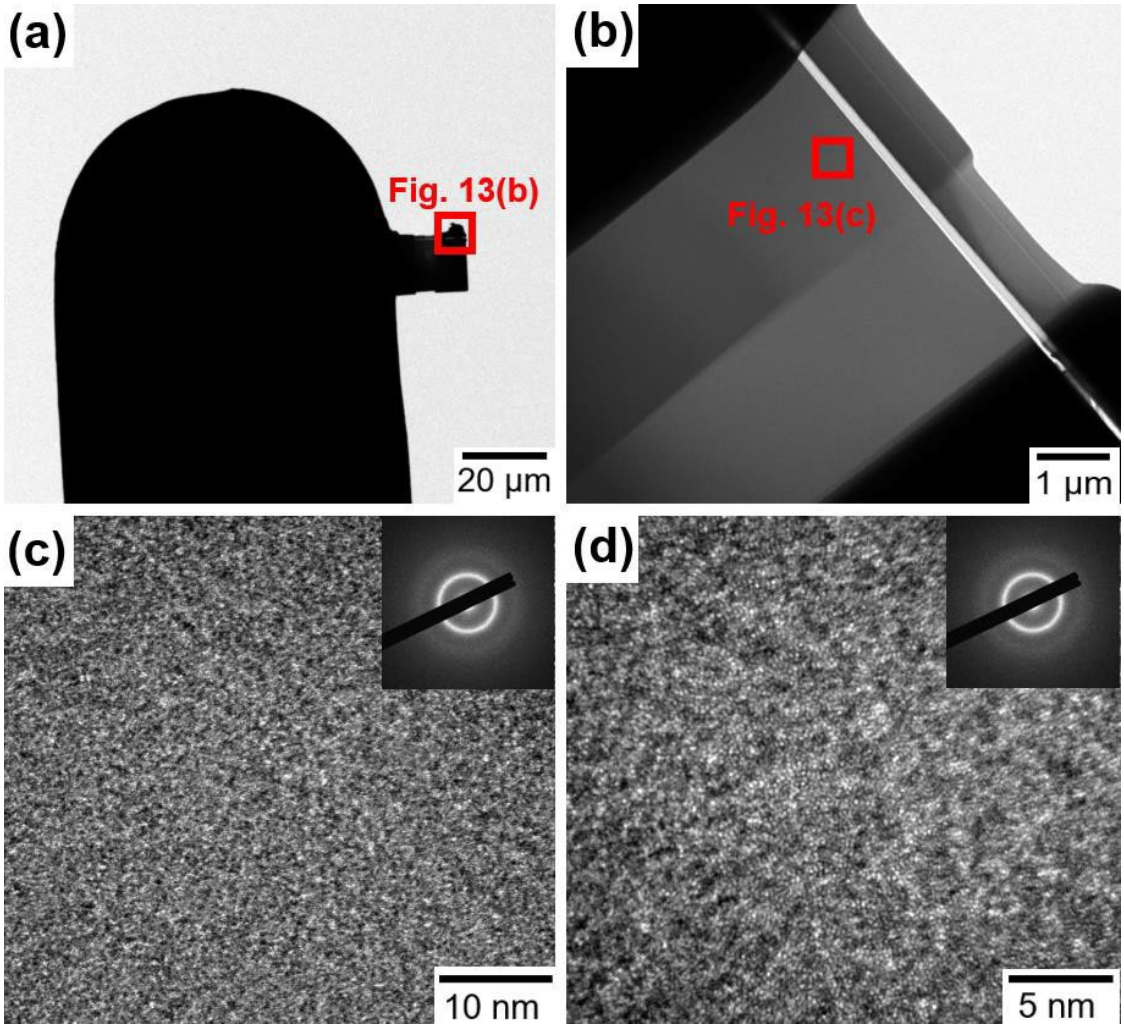


**Fig. 13** TEM results of BMG sample fabricated from crystalline foil.

## 4. Conclusion

In this study, the crystalline metallic glass foil was successfully utilized as feedstock for fabricating bulk metallic glass (BMG) using the Laser Foil Printing (LFP) process. Through remelting the crystalline foil with LFP, the fabrication of amorphous BMG was achieved. The XRD results indicate that using spot pattern welding with 500 W laser power, 0.65 ms spot duration time, and 150 μm spot distance could remelt the crystalline phase and oxidations to achieve an amorphous structure.

The decrease in glass-forming ability (GFA) of the crystalline foil was evident during the fabrication of BMG from the crystalline foil. The SEM images exhibit surface defects attributed to the poor GFA. In the microhardness results, two LFP-fabricated BMG samples show similar values around 490 HV due to the same process parameters. Further examination of BMG fabricated from crystalline foils was conducted through TEM. The amorphous structure was revealed with a halo ring in the selected area electron diffraction (SAED) pattern. Additionally, the bright-field (BF) images show no long-range ordered phase or crystalline lattice, indicating the amorphous structures of BMG parts.

## 5. References

[1] T. Zhang, X. Meng, C.Y. Wang, L. Li, J. Yang, W. Li, R.X. Li, Y. Zhang. Investigations of new bulk metallic glass alloys fabricated using a high-pressure die-casting method based on industrial grade Zr raw material. Journal of Alloys and Compounds. vol.792. 2019:851-859.

[2] O.Y. Di, P.C. Zhang, C. Zhang, L. Liu. Understanding of crystallization behaviors in laser 3D printing of bulk metallic glasses. Applied Materials Today. vol.23. 2021:100988.

[3] R.S. Khmyrov, P.A. Podrabinnik, T.V. Tarasova, et al. Partial crystallization in a Zr-based bulk metallic glass in selective laser melting. The International Journal of Advanced Manufacturing Technology. vol.126. 2023:5613-5631.

[4] Q. Jiang, P. Zhang, J. Tan, Z. Yu, Y.T. Tian, S.Y. Ma, D. Wu. Influence of the microstructure on mechanical properties of SLM additive manufacturing Fe-based bulk metallic glasses. Journal of Alloys and Compounds. vol.894. 2022:162525.

[5] F. Xie, Q. Chen, J. Gao, et al. Laser 3D Printing of Fe-Based Bulk Metallic Glass: Microstructure Evolution and Crack Propagation. Journal of Materials Engineering and Performance. vol.28. 2019:3478-3486.

[6] Y. Li, Y. Shen, C.H. Hung, M. C. Leu, H.L. Tsai. Additive manufacturing of Zr-based metallic glass structures on 304 stainless steel substrates via V/Ti/Zr intermediate layers. Materials Science and Engineering: A. vol.729. 2018:185-195.

[7] Y. Shen, Y. Li, C. Chen, H.L. Tsai. 3D printing of large, complex metallic glass structures. Materials & Design. vol.117. 2017:213-222.

[8] Y. Li, Y. Shen, M.C. Leu, H.L. Tsai. Mechanical properties of Zr-based bulk metallic glass parts fabricated by laser-foil-printing additive manufacturing. Materials Science and Engineering: A. 2019: 404-411.

[9] Y. Li, Y. Shen, C. Chen, M.C. Leu, H.L. Tsai. Building metallic glass structures on crystalline metal substrates by laser-foil-printing additive manufacturing. Journal of Materials Processing Technology. vol.248. 2017:249-261.

[10] Y. Li, Y. Shen, M.C. Leu, H.L. Tsai. Building Zr-based metallic glass part on Ti-6Al-4V substrate by laser-foil-printing additive manufacturing. Acta Materialia. vol.144. 2018:810-821.

[11] P. Bordeenithikasem, Y. Shen, H.L. Tsai, D.C. Hofmann. Enhanced mechanical properties of additively manufactured bulk metallic glasses produced through laser foil printing from continuous sheetmetal feedstock. Additive Manufacturing. vol.19. 2018:95-103.

[12] C.H. Hung, A. Sutton, Y. Li, Y. Shen, H.L. Tsai, M.C. Leu. Enhanced mechanical properties for 304L stainless steel parts fabricated by laser-foil-printing additive manufacturing. Journal of Manufacturing Processes. vol.45. 2019:438-446.

[13] P.N. Zhang, J.F. Li, Y. Hu, Y.H. Zhou. Microstructural evolution during annealing and rolling Zr52.5Cu17.9Ni14.6Al10Ti5 bulk metallic glass. Materials Science and Engineering: A. vol.499(1). 2009:374-378.
[14] R.C. Budhani, T.C. Goel, K.L. Chopra. Melt-spinning technique for preparation of metallic glasses. Bulletin of Materials Science. vol.4. 1982:549-561.
[15] W.H. Zhou, F.H. Duan, Y.H. Meng, C.C. Zheng, H.M. Chen, A.G. Huang, Y.X. Wang, Y. Li. Effect of alloying oxygen on the microstructure and mechanical properties of Zr-based bulk metallic glass. Acta Materialia. vol.220. 2021:117345.
[16] M. Mohr, R. K.Wunderlich, D.C. Hofmann, H.J. Fecht. Thermophysical properties of liquid $Zr_{52.5}Cu_{17.9}Ni_{14.6}Al_{10}Ti_5$—prospects for bulk metallic glass manufacturing in space. npj Microgravity. vol.5. 2019:24.
[17] E. Pekarskaya, J.F. Löffler, W.L Johnson. Microstructural studies of crystallization of a Zr-based bulk metallic glass. Acta Mater. 51 (2003) 4045-4057. https://doi.org/10.1016/S1359-6454(03)00225-8.